Angewandte Chemie
Eine Zeitschrift der Gesellschaft Deutscher Chemiker

Supporting Information

Anode-Free Lithium Metal Batteries Based on an Ultrathin and Respirable Interphase Layer

Y. Wang, Z. Qu, S. Geng, M. Liao, L. Ye, Z. Shadike, X. Zhao, S. Wang, Q. Xu, B. Yuan, X. Zhang, X. Gao, X. Jiang, H. Peng, H. Sun**

Experimental

Preparation of TEG-Cu current collector. Triethylamine germanate (TEG) was prepared *via* a one-step reaction[1]. Typically, 0.5 g of commercial GeO_2 powder (Aldrich, 99.99%) and 0.75 mL of triethylamine (TEA, Aldrich Reagent Co. Ltd, 99.8%) were added into a mixed solution of deionized water (1 mL) and 4 mL anhydrous ethanol (Aldrich, 99.8%), followed by stirring for 1 h at 25 °C to obtain a transparent solution. The TEG-Cu current collector was prepared by drop-casting the TEG solution on a Cu foil (8 cm×10 cm, thickness of 9 μm) using a stainless-steel blade, followed by drying at 80 °C under vacuum for 1 h, and the mass loading of TEG on Cu foil was measured to be ~0.05 mg cm^{-2}. The TEG-Cu current collectors with different thicknesses were prepared by varying the concentration of TEG solution from 0.05 M to 0.2 M. The TEG-Cu and Cu current collectors were punched into discs with a diameter of 12 mm for electrochemical measurement and characterization.

Electrochemical measurements. All the cells were assembled in an argon-filled glove box with H_2O < 1 ppm and O_2 < 1 ppm. To prepare Li/Cu coin cells (2032-type), bare Cu or TEG-Cu current collector was paired with a Li metal foil and one layer of glass fibre membrane (Whatman, GF/A), which was dried at 120 °C under vacuum for 48 h before use. The electrolyte was 1 M lithium bis(trifluoromethanesulfonyl)imide (LiTFSI) was dissolved in the mixture of 1,3-dioxolane/1,2-dimethoxyethane (DOL/DME, 8/2 in volume) with 3 wt% lithium nitrate ($LiNO_3$) and purified by activated molecular sieves for 24 h before use. All assembled half cells were aged for 6 h and then tested on a Neware battery testing system (CT-4008-5V50mA-164-U). Galvanostatic Li plating/stripping was conducted under increasing current densities from 0.5 to 5 mA cm^{-2} and plating capacities from 0.5 to 2 mAh cm^{-2}. Aurbach tests were carried out by pre-plating 5 mAh cm^{-2} Li metal first, and galvanostatic plating/stripping for 10 cycles at a current density of 1 mA cm^{-2} and a plating capacity of 1 mAh cm^{-2}. Li/Li symmetrical cells were prepared and tested under the same condition with Li/Cu cells. EIS measurements were performed on the electrochemical workstation (CHI660E) with increasing frequencies from 100 kHz to 0.01 Hz and an amplitude at 5 mV. CV profiles were carried out on the electrochemical workstation (CHI660E) at the scan rate of 0.1 mV s^{-1}. Anode-free full cells were assembled using a TEG-Cu or Cu current collector and commercial $LiFePO_4$ cathode (~16 mg cm^{-2}). Galvanostatic charge/discharge measurement was conducted with a voltage range from 2.0 to 3.8 V at a current density of 17 mA g^{-1} for the initial 3 cycles, accompanied with a charge and discharge current density of 51 and 85 mA g^{-1} in the following

cycles, respectively. The specific capacity, energy and powder densities were calculated based on the mass of the LFP. All the electrochemical measurements were performed at 28 ºC in a thermostatic test chamber (Neware MHW-200).

Physical characterization. SEM was performed on a ZEISS Gemini 300 Field Emission Scanning Electron Microscopy with an accelerating voltage of 15 kV. The EDS mapping was conducted with the electron beam condition of 5 kV and 1.6 nA. TEM was conducted on a JEOL JEM-2100F transmission electron microscope at 200 kV. The XRD patterns were acquired using a Rigaku Ultima IV powder X-ray diffractometer with Cu Kα radiation. For the time-of-flight secondary-ion mass spectrometry (TOF-SIMS) studies, ION-TOF TOF-SIMS 5 was used under the pressure of analysis chamber below 1.1×10^{-9} mbar. The organic imaging with delay extraction mode with pulsed 30 keV Bi^{3+} (0.27 pA pulsed current) ion beam was applied for depth profiling analysis with 1 keV Cs^{+} ion beam sputtering at the same time (69.27–82.74 nA current) and 300 × 300 μm^2 sputter raster. The analysis area is 50 × 50 μm^2. Fourier transform infrared spectroscopy (FTIR) was conducted on Fourier transform infrared spectrometer (Nicolet 560). Atomic force microscope (AFM) nanomechanical measurement was conducted on Oxford MFP-3D AFM to characterize the the topopraphy and mechanical properties of the SEI formed on Cu current collectors. XPS scans were recorded on an Thermo Fisher Nexsa XPS Microprobe operated at 25 mA and 15 kV to characterize the surface composition. All the binding energies were calibrated with the C1s peak (284.8 eV). Raman spectra were measured by Renishaw inVia Qontor instrument with a 520 nm Ar ion laser.

Calculation of the energy densities. Based on the total mass of active materials on both cathode and anode, the energy density (*E*) of anode-free LMB can be calculated as follows[2-4]:

$$E = \frac{U_{avg} * C}{m_{cathode} + m_{anode}}$$

U_{avg} is the discharge voltage (*e.g.*, 3.40 V); *C* is the discharge capacity (*e.g.*, 2.63 mAh cm^{-2}); $m_{cathode}$ and m_{anode} represent the active materials on cathode (*e.g.*, 16.9 mg cm^{-2} for LFP) and anode (*e.g.*, 0.05 mg cm^{-2} for TEG layer), respectively.

Supporting Figures

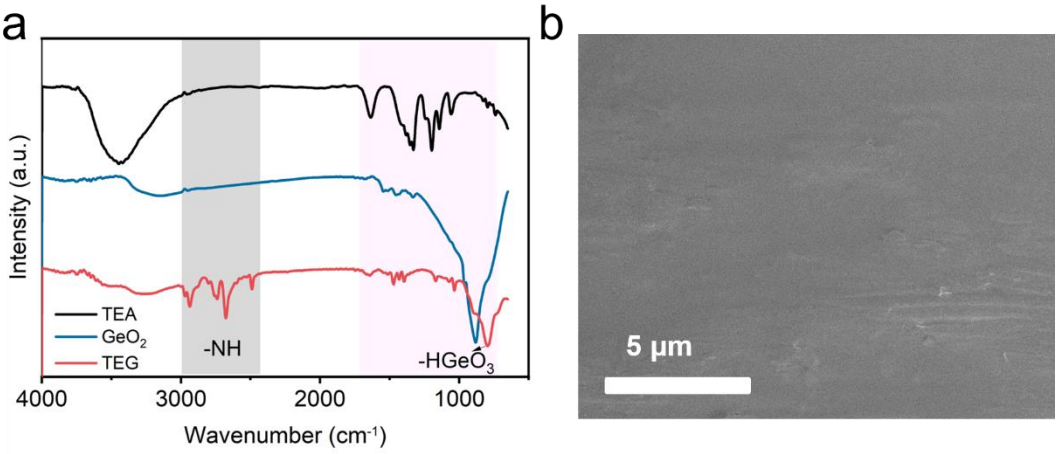

Fig. S1. (a) Fourier transform infrared spectroscopy of TEA, GeO_2 and TEG. **(b)** SEM image of the TEG-Cu current collector.

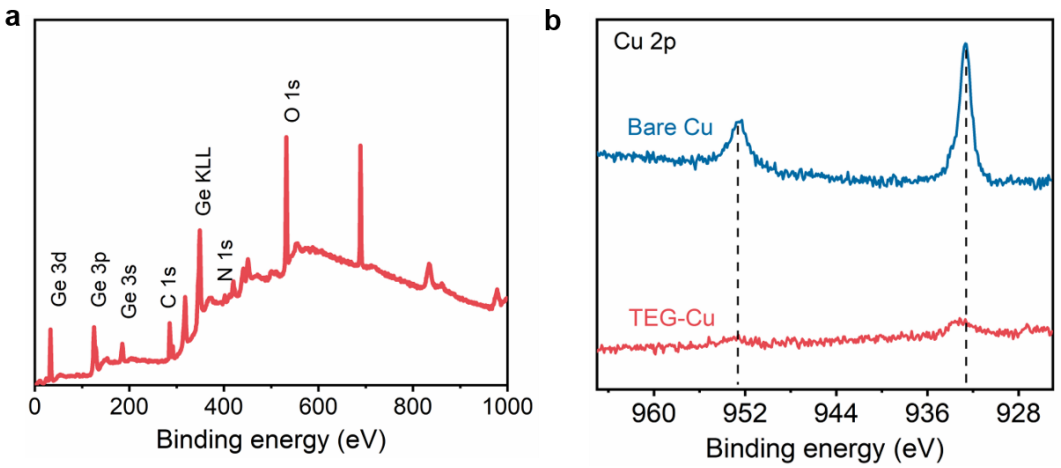

Fig. S2. (a) Wide-scan XPS spectrum for TEG-Cu. **(b)** High-resolution XPS spectra of Cu 2p for bare Cu and TEG-Cu.

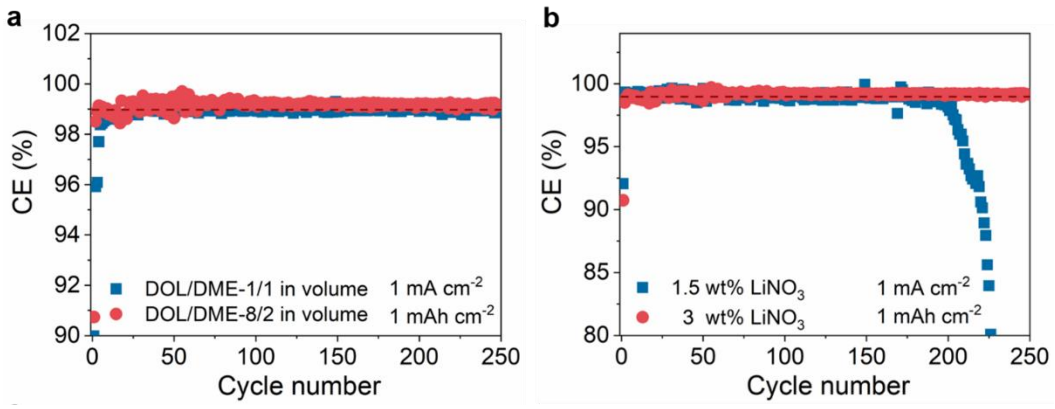

Fig. S3. Coulombic efficiencies of Li plating/stripping in Li/TEG-Cu cells using electrolytes with different **(a)** DOL/DME volume ratios and **(b)** $LiNO_3$ concentrations.

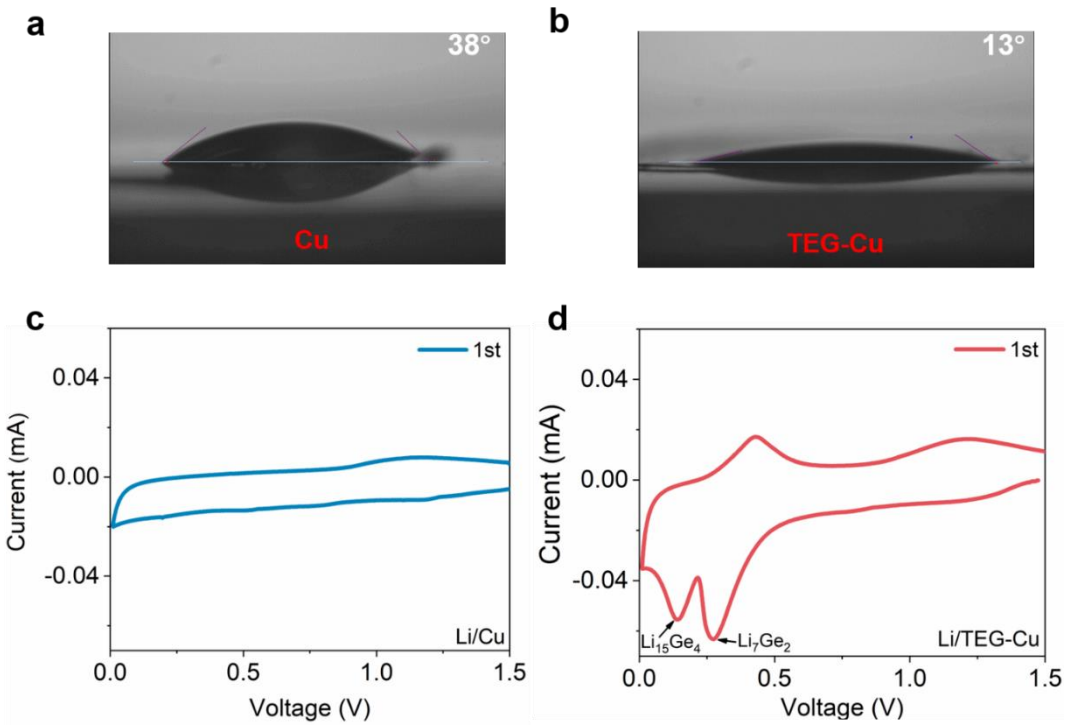

Fig. S4. (a-b) Contact angles of the electrolyte on **(a)** bare Cu and **(b)** TEG-Cu current collectors. **(c-d)** CV profiles of Li/Cu cells using with (**c**) bare Cu and (**d**) TEG-Cu at 0.1 mV s^{-1}.

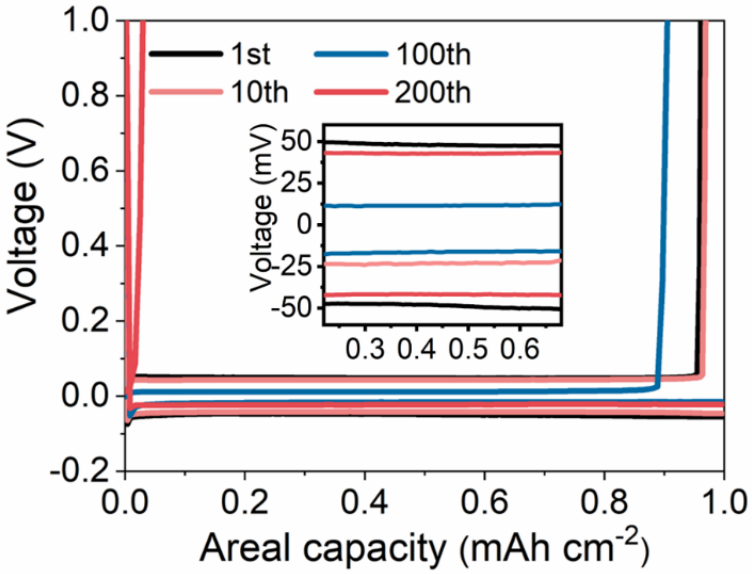

Fig. S5. Galvanostatic charge-discharge curves of Li/Cu cells cycled at 1 mA cm^{-2} and 1 mAh cm^{-2}.

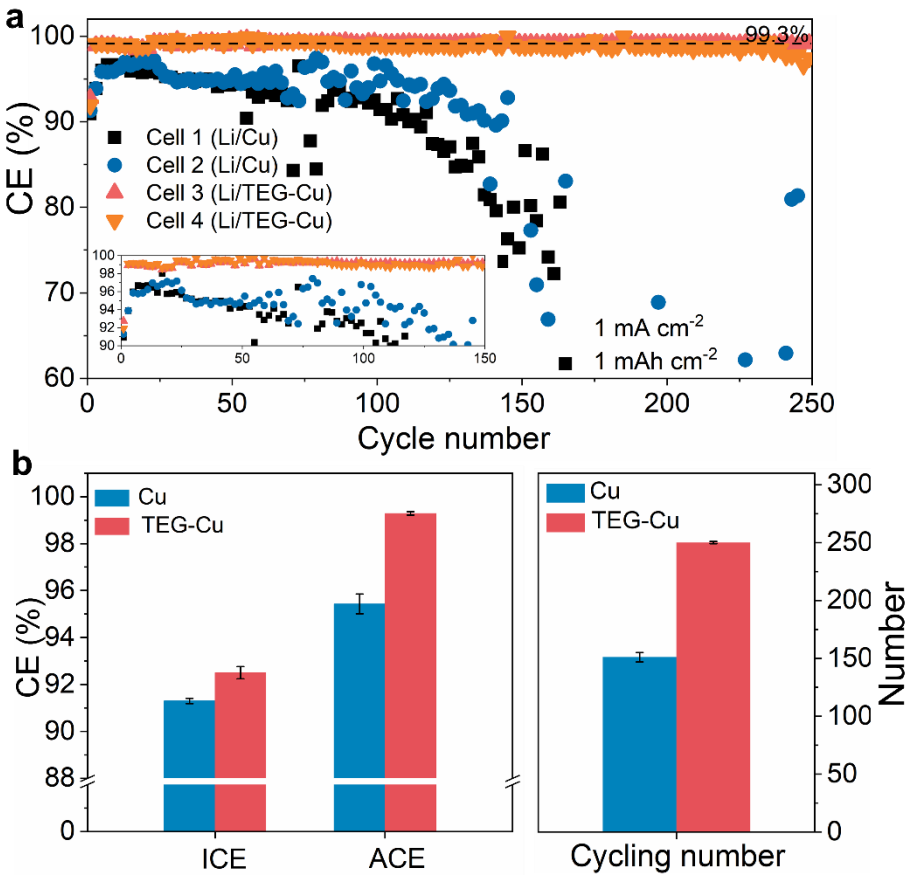

Fig. S6. (a) Coulombic efficiencies of Li plating/stripping in multiple Li/Cu and Li/TEG-Cu cells at 1 mA cm^{-2} and 1 mAh cm^{-2}. **(b)** Comparison of initial CE (ICE), average CE (ACE) and cycling number between Li/Cu and Li/TEG-Cu cells.

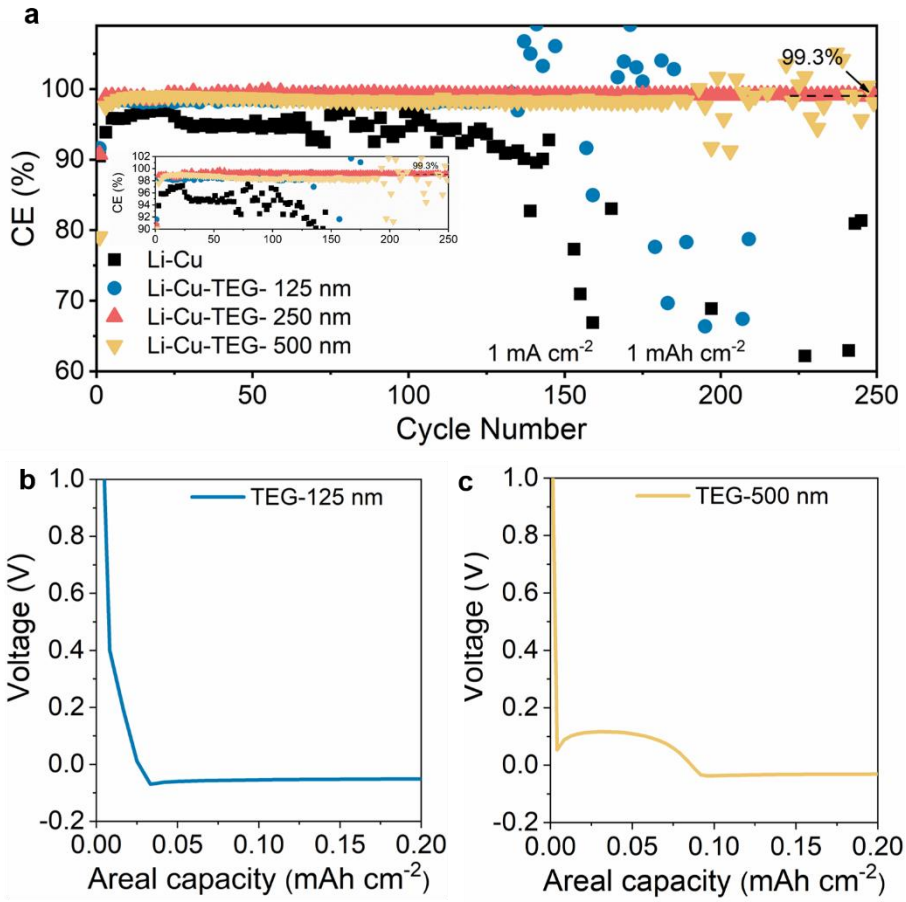

Fig. S7. (a) Coulombic efficiencies of Li plating/stripping in Li/Cu and Li/TEG-Cu cells with varied TEG thickness at 1 mA cm^{-2} and 1 mAh cm^{-2}. Voltage profiles of the initial Li deposition on TEG-Cu with the thickness of 125 nm **(b)** and 500 nm **(c)** at 1 mA cm^{-2}.

The thickness of TEG layer on the Cu current collector could be controlled by regulating the mass loading of TEG. As shown, both the TEG layers with the thicknesses of ~125 nm and ~500 nm showed inferior cycle numbers and CEs for Li plating/stripping than that of 250 nm.

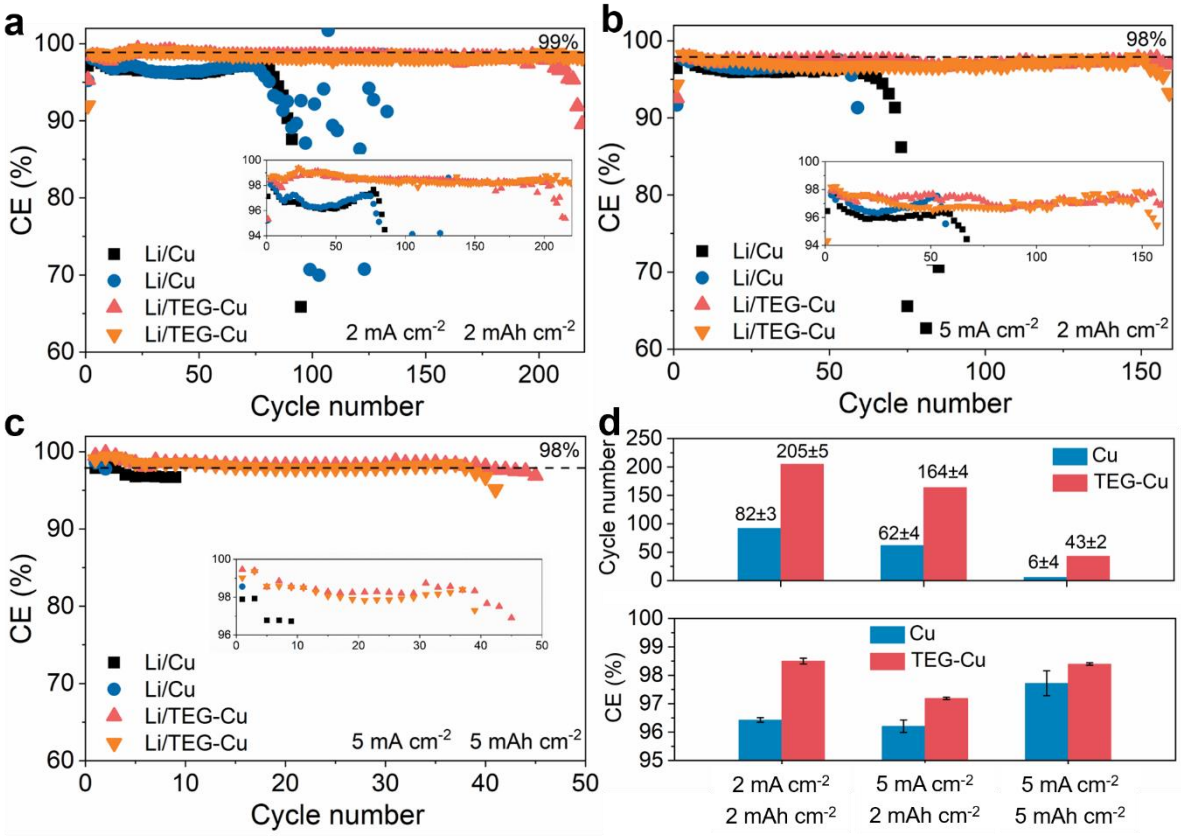

Fig. S8. Coulombic efficiencies of Li plating/stripping in multiple Li/Cu and Li/TEG-Cu cells at **(a)** 2 mA cm^{-2} and 2 mAh cm^{-2}, **(b)** 5 mA cm^{-2} and 2 mAh cm^{-2}, and **(c)** 5 mA cm^{-2} and 5 mAh cm^{-2}. **(d)** Comparison of the average CE and cycle number between Li/Cu and Li/TEG-Cu cells.

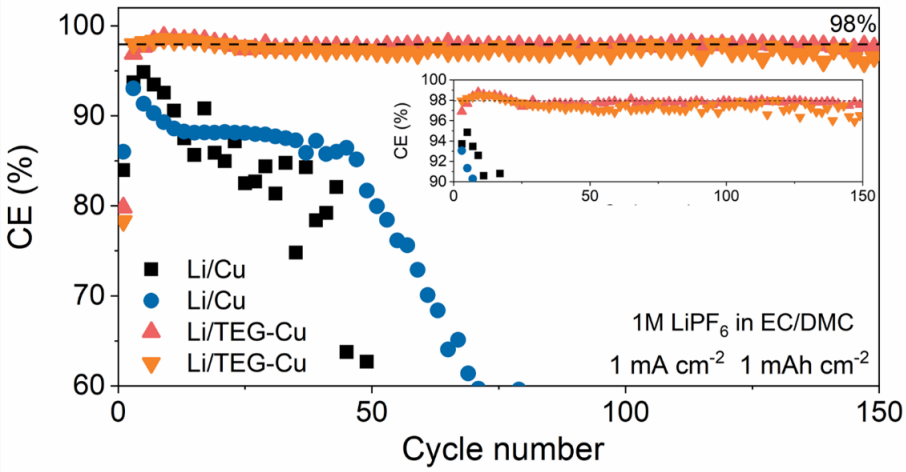

Fig. S9. Coulombic efficiencies of Li plating/stripping in multiple Li/Cu and Li/TEG-Cu cells using a commercial carbonate electrolyte comprised of 1 M $LiPF_6$ in EC/DMC (1/1 in volume) at 1 mA cm^{-2} and 1 mAh cm^{-2}.

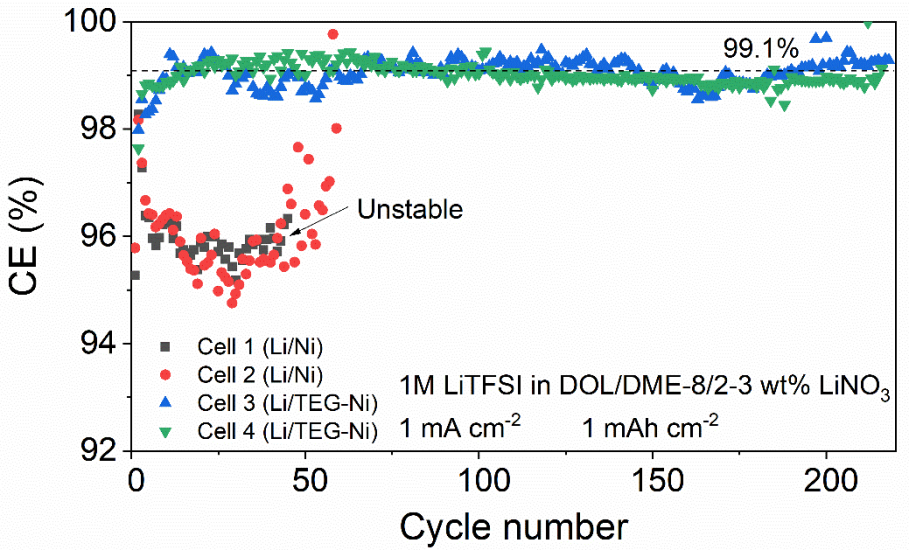

Fig. S10. Coulombic efficiencies of Li plating/stripping in Li/Ni and Li/TEG-Ni cells at 1 mA cm^{-2} and 1 mAh cm^{-2}.

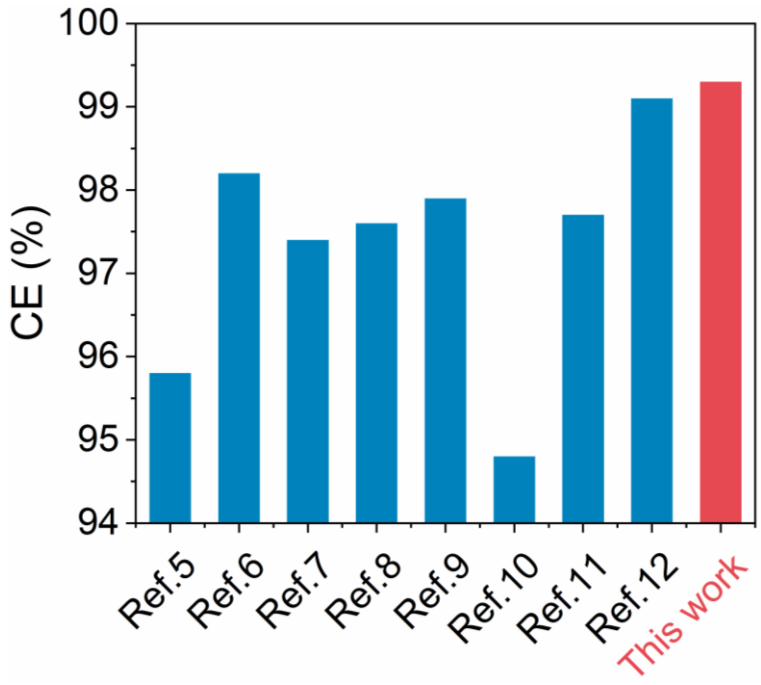

Fig. S11. Comparison of Li plating/stripping Coulombic efficiencies based on Aurbuch test in our Li/TEG-Cu and state-of-the-art Li/Cu cells.

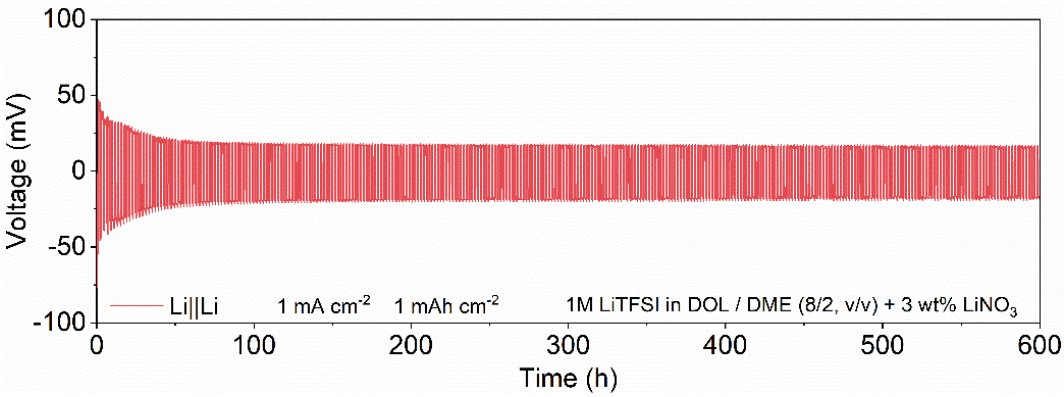

Fig. S12. Li/Li symmetric cells based on the modified electrolytes at 1 mA cm^{-2} and 1 mAh cm^{-2}.

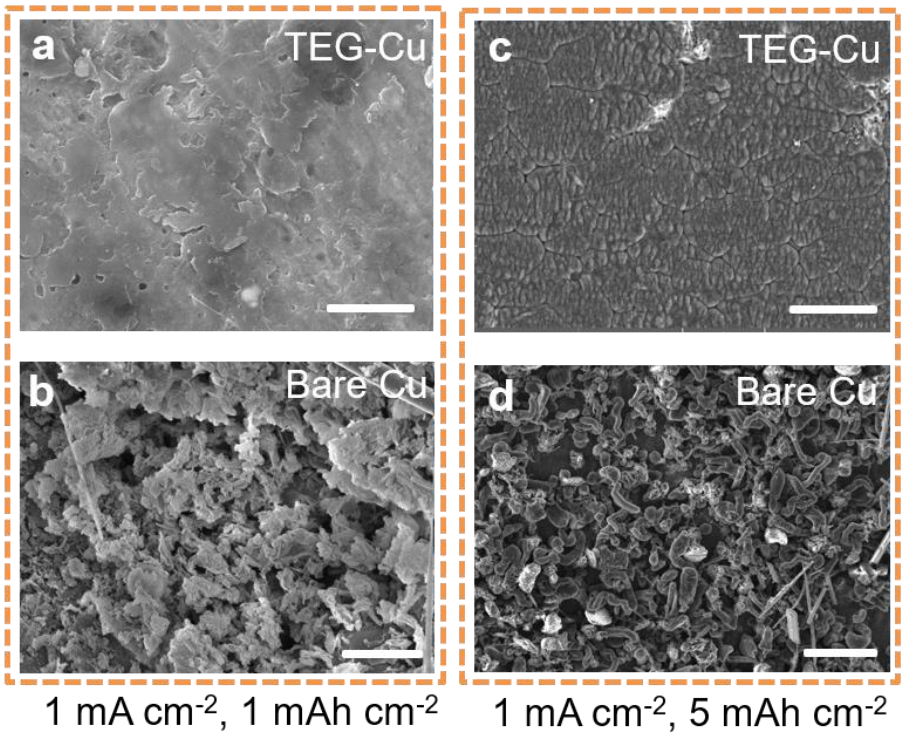

Fig. S13. SEM images of Li deposition on bare Cu and TEG-Cu current collectors. Scale bars in **(a, c)** 5 μm. Scale bars in **(b, d) 10** μm.

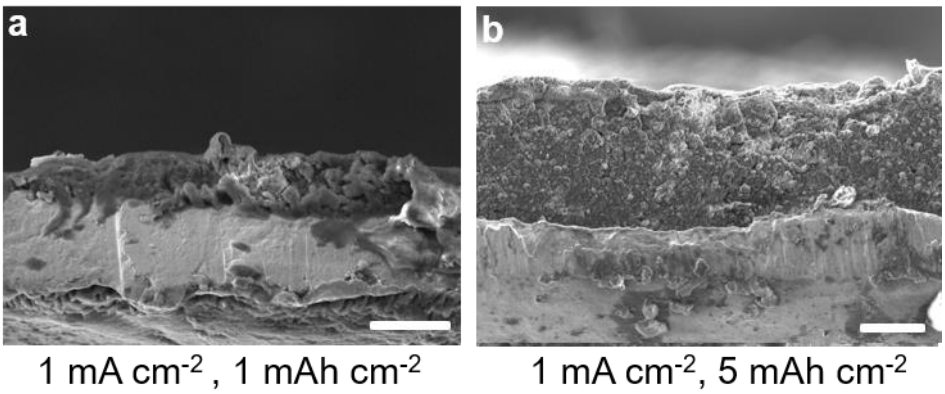

Fig. S14. Cross-sectional SEM images of Li deposition on bare Cu at **(a)** 1 mA cm^{-2} and 1 mAh cm^{-2} and **(b)** 1 mA cm^{-2} and 5 mAh cm^{-2}. Scale bars in **(a)**, 10 μm. Scale bars in **(b)**, 20 μm.

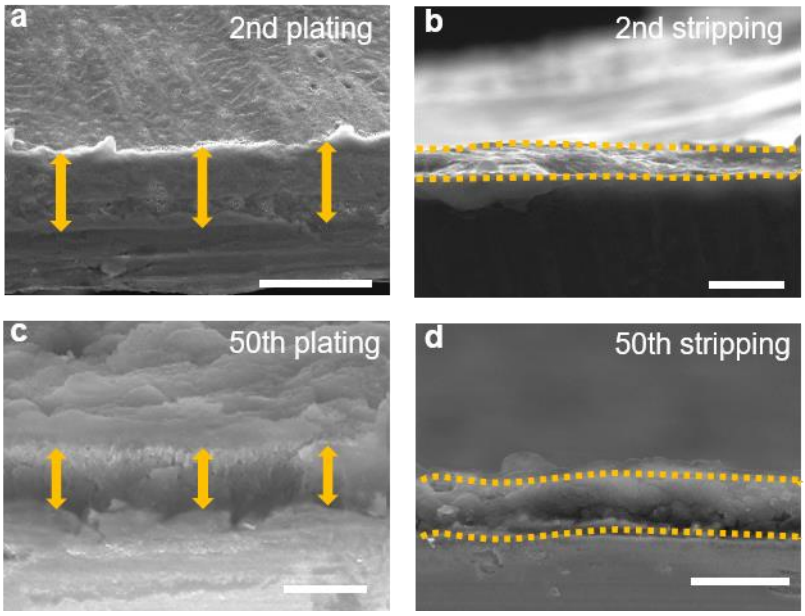

Fig. S15. (a, b) Cross-sectional SEM images of TEG-Cu after the 2nd Li plating and stripping at 1 mA cm^{-2} and 1 mAh cm^{-2}, respectively. **(c, d)** Cross-sectional SEM images of TEG-Cu after the 50th Li plating and stripping, respectively. Scale bars in **(a**, **c)** 10 μm. Scale bars in **(b**, **d)** 1 μm.

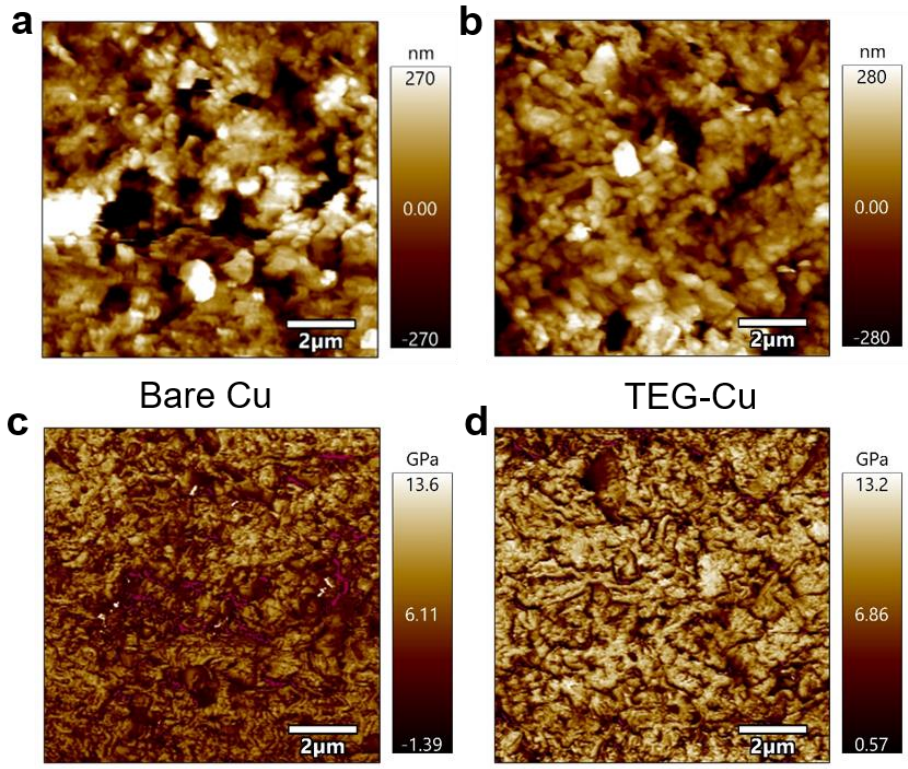

Fig. S16. (a, b) AFM topography of the interphase layers formed on bare Cu and TEG-Cu, respectively. **(c, d)** Young's modulus distribution of the interphase layers formed on bare Cu and TEG-Cu, respectively. All the samples were cycled at 1 mA cm^{-2} and 1 mAh cm^{-2} for 10 cycles, and stopped after Li stripping.

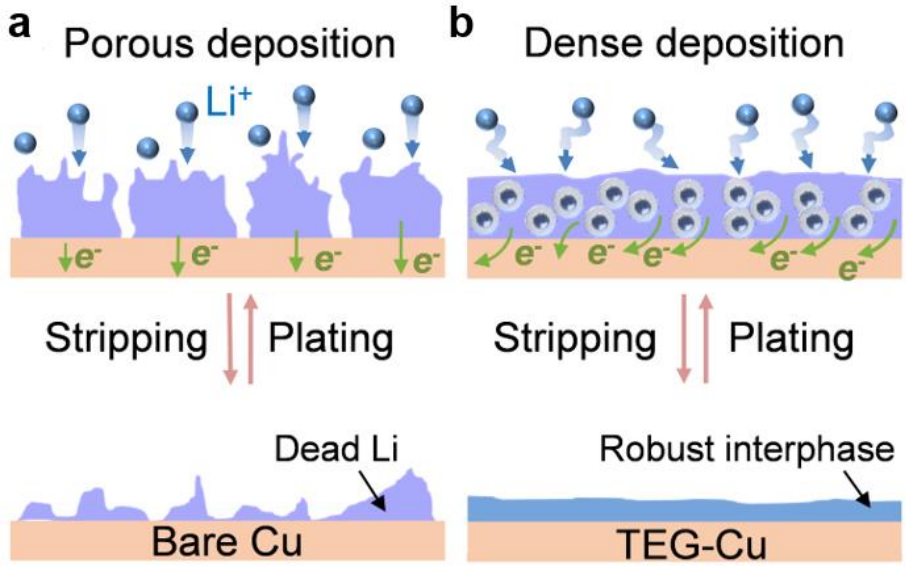

Fig. S17. (a, b) Schematic illustration of the morphology evolution of Li deposition layer during repeated plating/stripping on bare Cu and TEG-Cu, respectively.

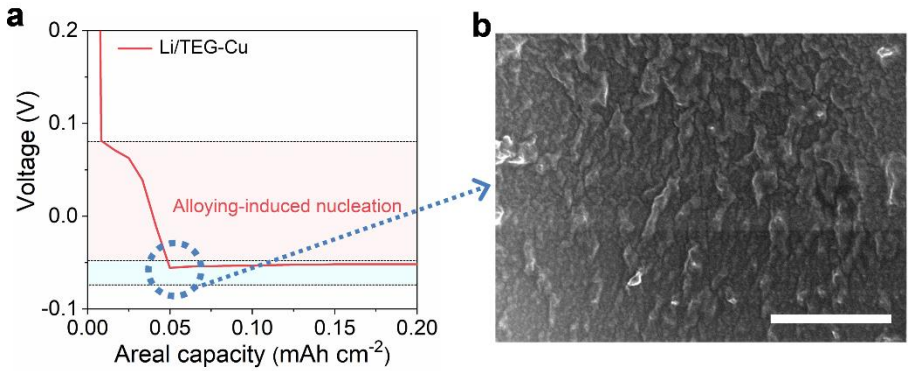

Fig. S18. (a) Voltage profiles of the initial Li deposition on TEG-Cu at 1 mA cm^{-2}. **(b)** SEM image of the TEG-Cu after initial Li deposition for 0.05 mAh cm^{-2}. Scale bar, 10 μm.

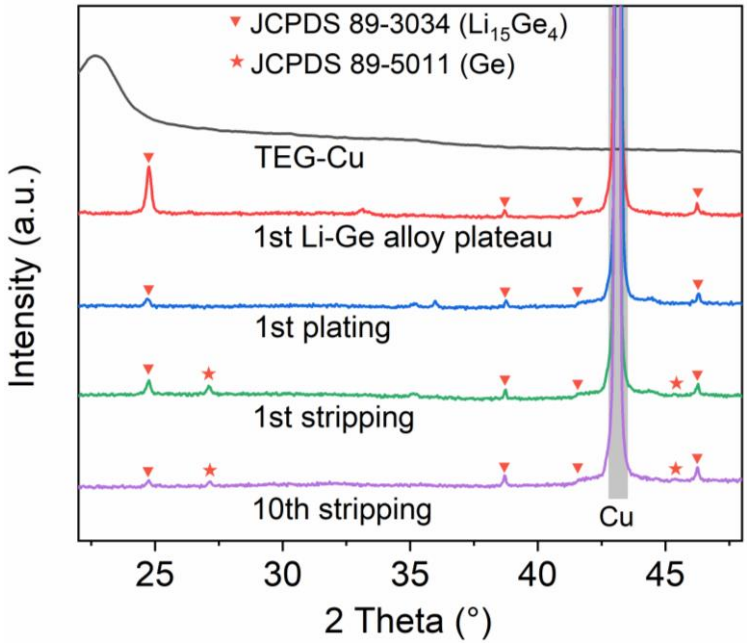

Fig. S19. *Ex-situ* XRD spectra of the pristine TEG-Cu and after the first Li-Ge alloy plateau, after the first Li plating, after the first Li stripping, and after 10 cycles stopped at the fully stripping state.

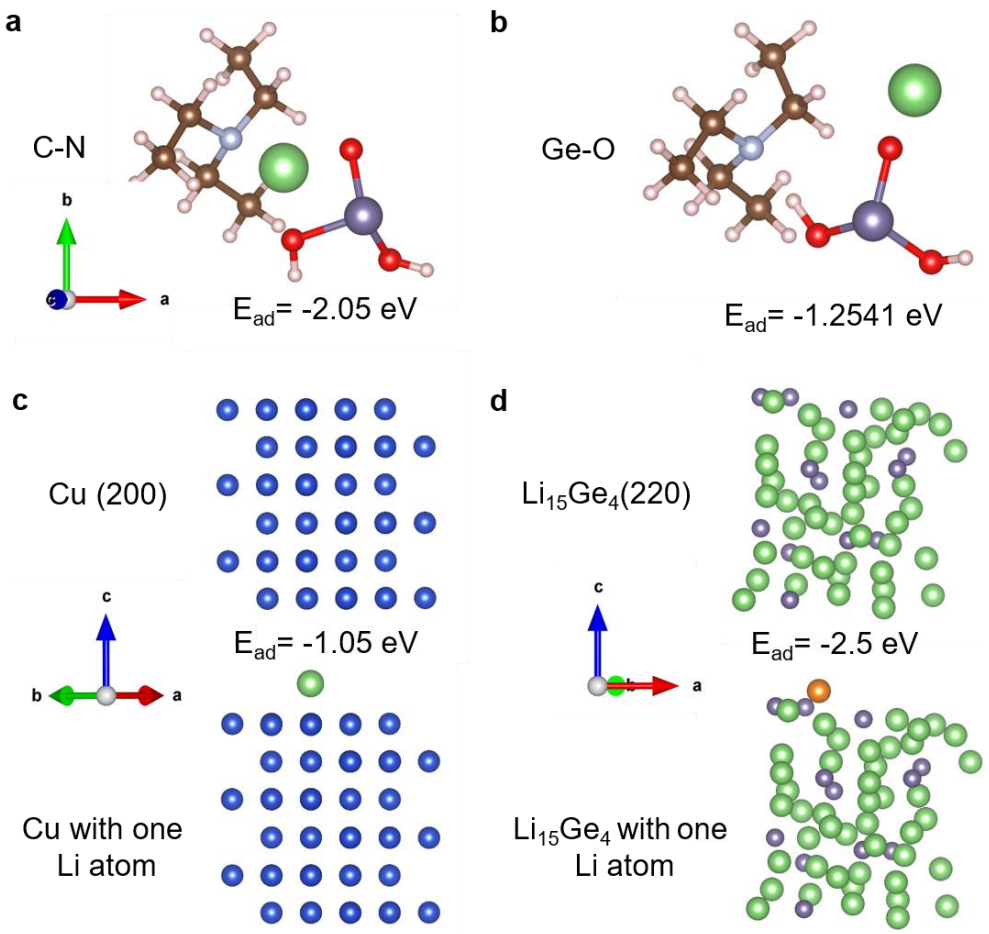

Fig. S20. (a, b) Calculated adsorption energy between Li and C-N and Ge-O, respectively. **(c)** Calculated adsorption energy between Li and Cu. **(d)** Calculated adsorption energy between Li and $Li_{15}Ge_4$.

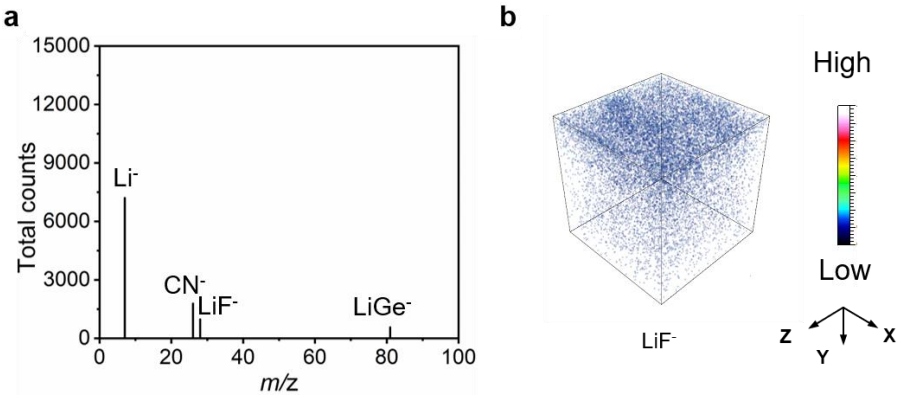

Fig. S21. (a) TOF-SIMS spectra of CN^-, $LiGe^-$, Li^-, LiF^- and secondary ion fragments obtained by sputtering of the initial Li deposition on TEG-Cu at 1 mA cm^{-2} and 1 mAh cm^{-2}. **(b)** Three-dimensional distributions of LiF^- constructed based on TOF-SIMS depth scan of the TEG-Cu after Li plating. Analysis area is 50 × 50 μm^2.

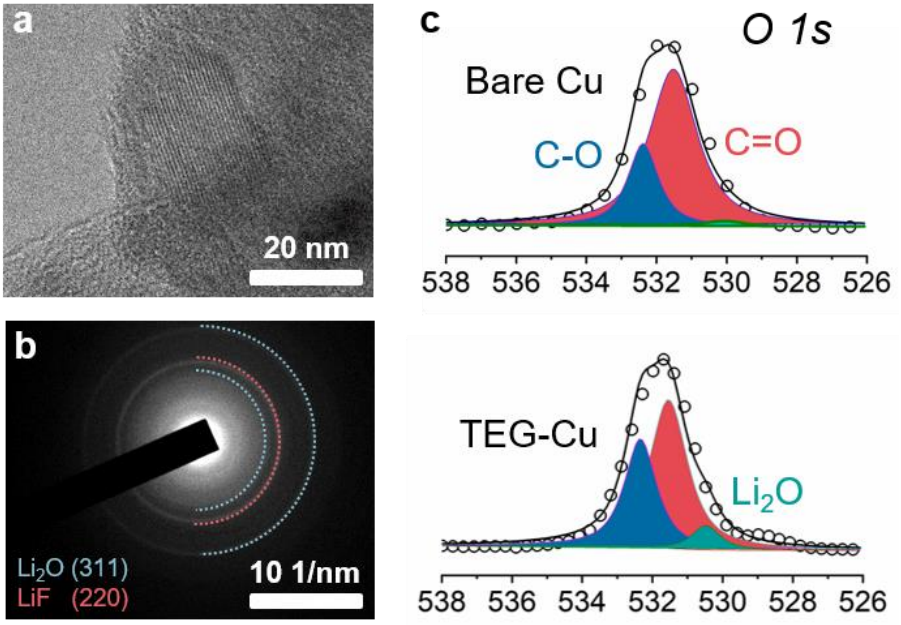

Fig. S22. (a, b) High-resolution TEM images and SAED pattern of TEG-Cu after Li-plating, respectively. **(c)** High-resolution XPS spectra for O 1s of the Li deposition on bare Cu and TEG-Cu after 20 cycles at 1 mA cm^{-2} and 1 mAh cm^{-2}.

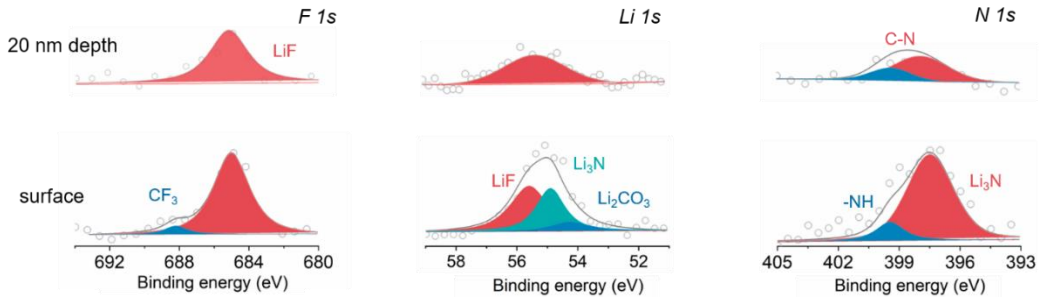

Fig. S23. High-resolution XPS depth profiles of F 1s, Li 1s and N 1s spectra of Li deposition on TEG-Cu after 20 cycles at 1 mA cm^{-2} and 1 mAh cm^{-2}.

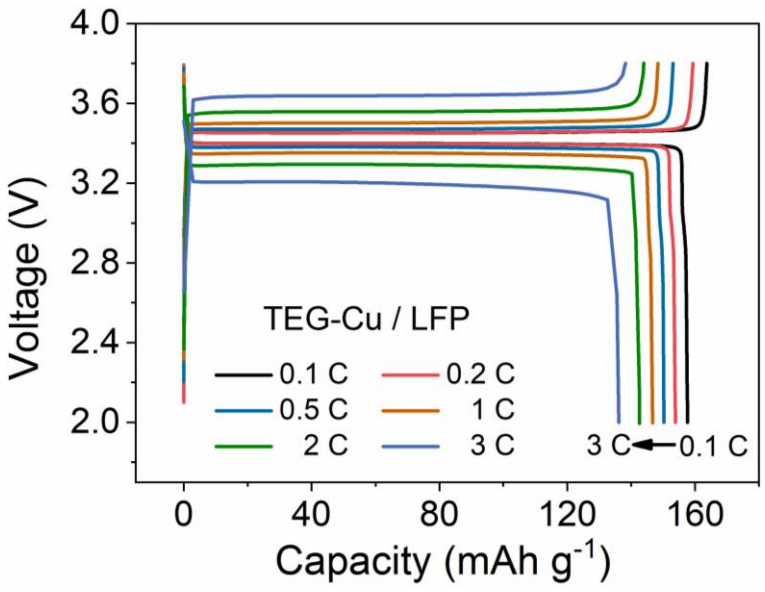

Fig. S24. Galvanostatic charge-discharge curves of the anode-free TEG-Cu/LFP battery cycling at increasing rates from 0.1 to 3 C. Areal capacity, 3 mAh cm^{-2}.

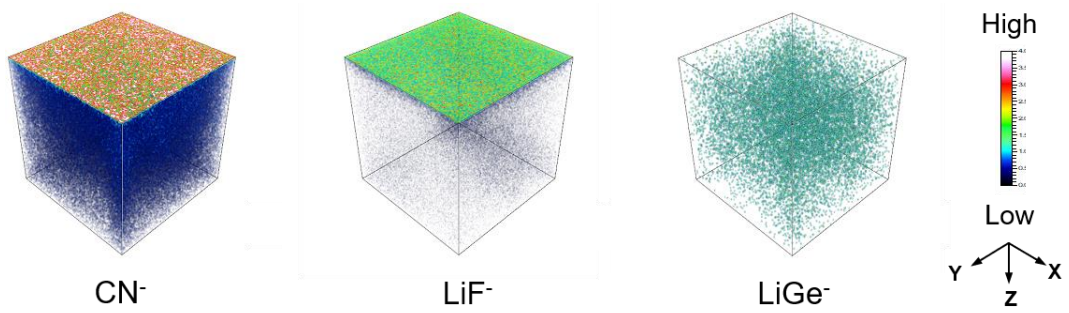

Fig. S25. Three-dimensional distribution of CN^-, LiF^-, and $LiGe^-$ based on TOF-SIMS depth scan of the TEG-Cu after Li plating in anode-free TEG-Cu/LFP. Current density and areal capacity, 1.36 mA cm^{-2} and 3 mAh cm^{-2}, respectively. The analysis area is 50 × 50 μm^2.

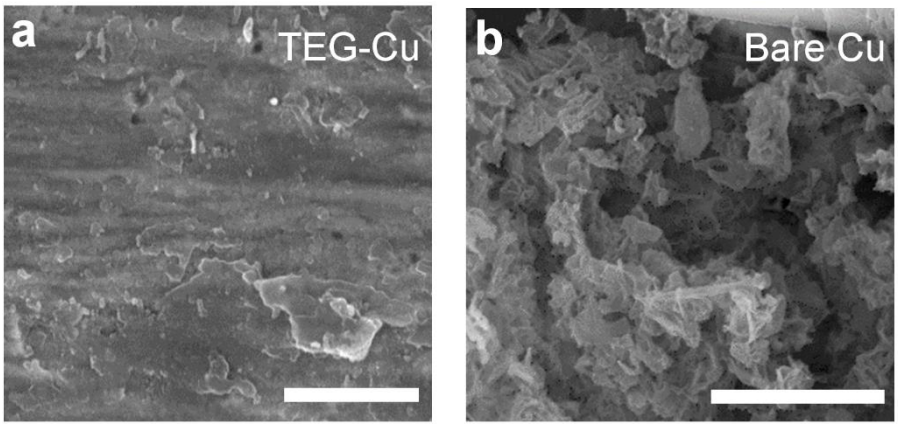

Fig. S26. (a, b) SEM images of Li deposition on TEG-Cu and bare Cu after 100 cycles in anode-free LFP full cells. Current density and areal capacity, 1.36 mA cm^{-2} and 3 mAh cm^{-2}, respectively. Scale bars, 10 μm.

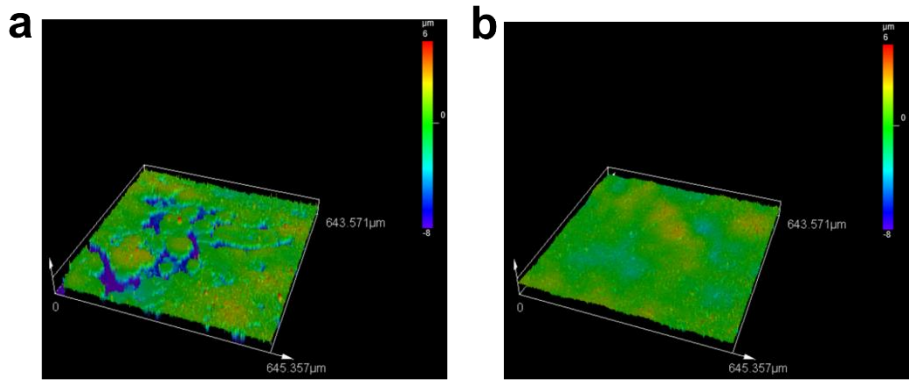

Fig. S27. (a, b) Three-dimensional distribution constructed from laser confocal scanning microscopy images of Li deposition on **(a)** bare Cu and **(b)** TEG-Cu after 10 cycles in anode-free LFP full cells. Current density and areal capacity, 1.36 mA cm^{-2} and 3 mAh cm^{-2}, respectively.

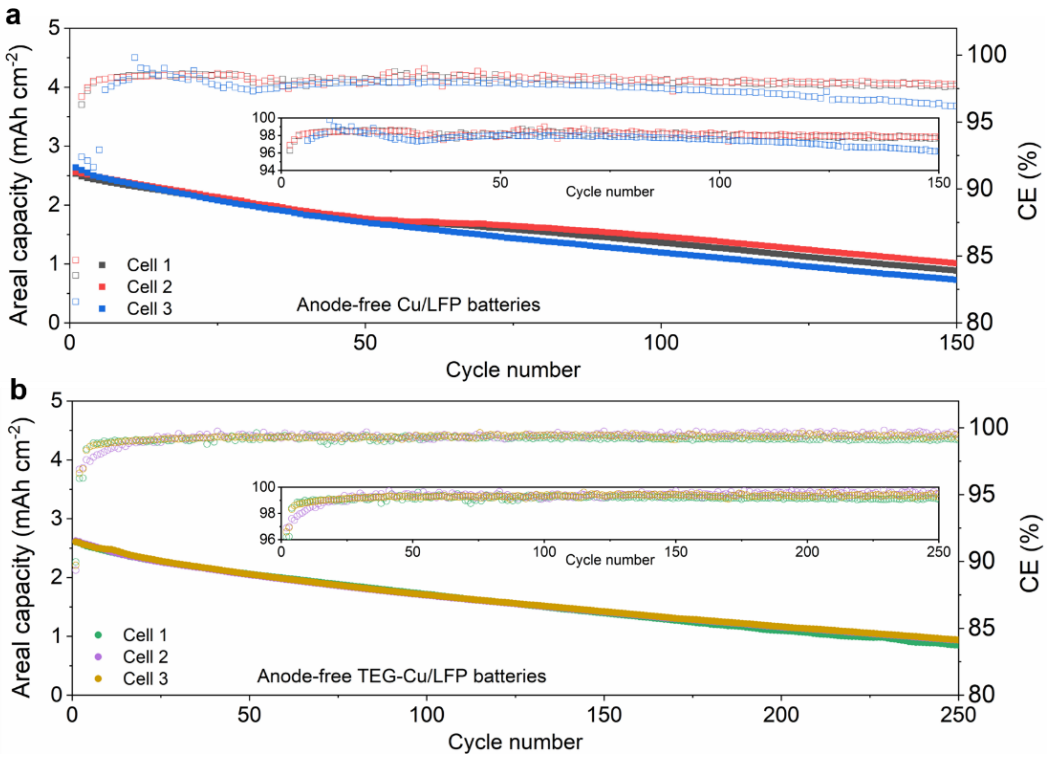

Fig. S28. Cycling performances of multiple anode-free **(a)** Cu/LFP and **(b)** TEG-Cu/LFP cells under the same fabrication and characterization condition. Current density and areal capacity, 1.36 mA cm^{-2} and 3 mAh cm^{-2}, respectively.

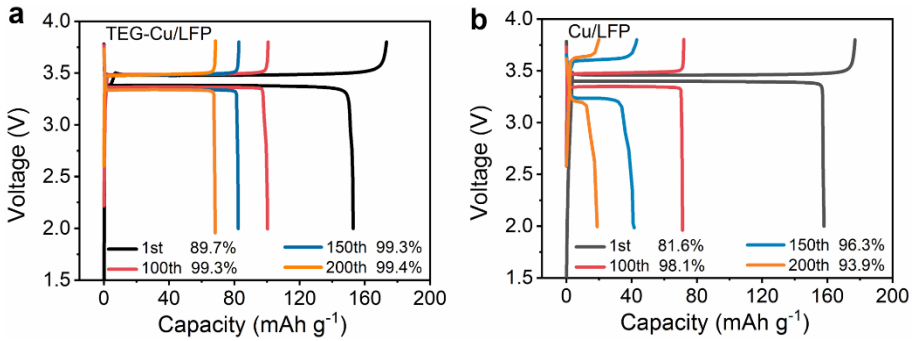

Fig. S29. Galvanostatic charge-discharge curves of the anode-free TEG-Cu/LFP **(a)** and Cu/LFP batteries **(b)** at the 1st, 100th, 150th and 200th cycles. Areal capacity, 1.36 mA cm^{-2} and 3 mAh cm^{-2}, respectively.

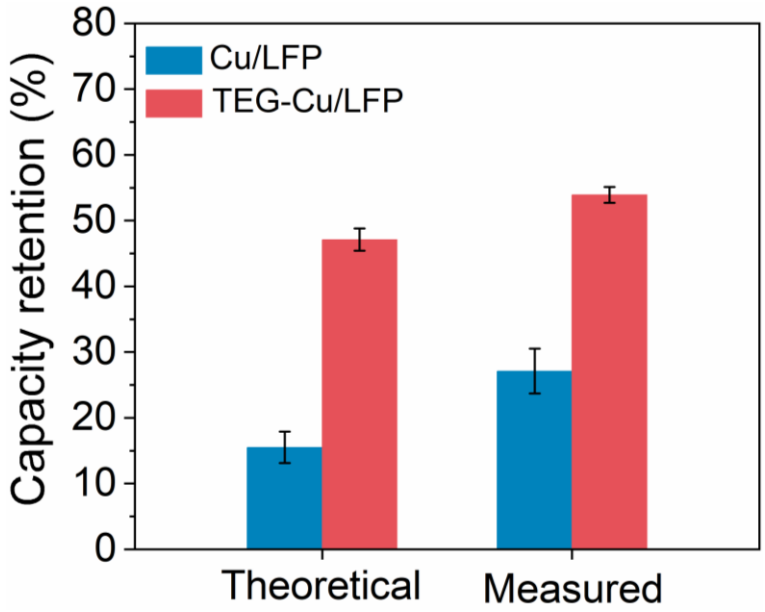

Fig. S30. Comparison of the theoretical and measured capacity retention of Cu/LFP and TEG-Cu/LFP anode-free batteries.

The theoretical capacity retention was calculated according to the formula as follows[13]:

$$\frac{Q_n}{Qi} = \prod_{i=2}^{n} CE_i$$

Where Q_n is the discharge capacity of an anode-free battery after n cycles, Q_i is the initial discharge capacity and CE_i is the Coulombic efficiency for cycle number i.

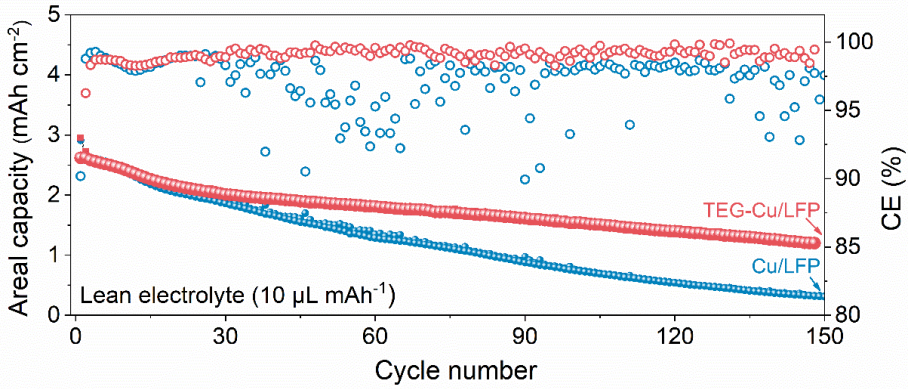

Fig. S31. Cycling performances of anode-free Cu/LFP and TEG-Cu/LFP batteries with the current density of 1.36 mA cm^{-2} and areal capacity of 3 mAh cm^{-2} under lean-electrolyte condition with an electrolyte-to-capacity (E/C) ratio of 10 μL mAh^{-1}.

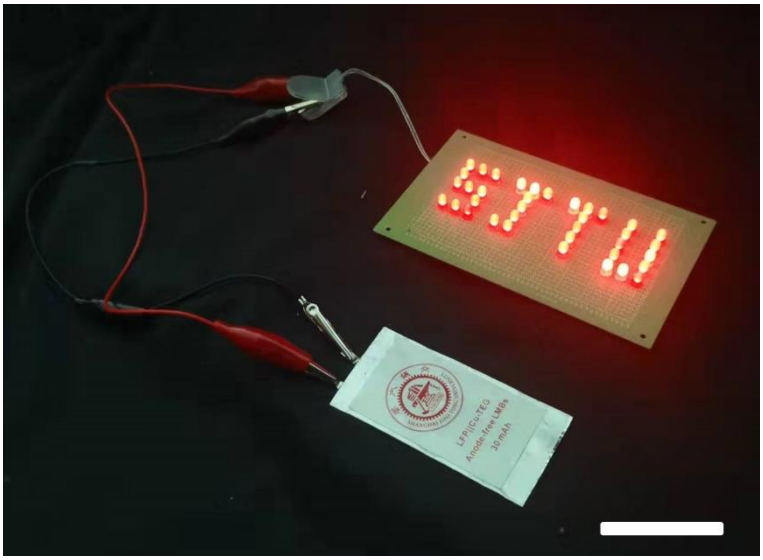

Fig. S32. An anode-free pouch cell readily lightening up an LED array comprised of 37 in-parallel LED lamps. Scale bar, 5 cm.

Supporting Tables

Table S1. Impedance parameters derived from the equivalent circuit model of Li/Cu and Li/TEG-Cu cells after the 1st and 50th cycles (stopped at fully discharged state).

	Ohmic resistance (R1 / Ω cm^{-2})	Charge-transfer resistance (R2 / Ω cm^{-2})
Li/Cu after the 1st cycle	4.11	50.0
Li/Cu after the 50th cycle	6.75	80.4
Li/TEG-Cu after the 1st cycle	3.17	38.0
Li/TEG-Cu after the 50th cycle	3.57	40.8

Table S2. Comparison of the areal capacity and cycle number of our TEG-Cu/LFP and state-of-the-art anode-free LFP batteries.

Anode	Areal capacity (mAh cm^{-2})	Maximal current density (mA cm^{-2})	Cycle number	Capacity retention (%)	Ref.
Li-SiOx /Cu	1.1	0.9	200	~20	3
Cu	1.7	0.3	100	50	14
Cu	2.1	1.02	140	70	15
Cu	1.7	0.2	50	~55	16
Cu	1.0	0.4	50	40	17
PVDF-Cu	1.5	0.2	100	61	18
Cu-CuCl	1.6	1.05	100	78.4	19
Cu	1.5	0.5	100	48	20
Cu	2.5	–	150	43.8	21
TEG-Cu	**3**	**1.36**	**100** **150** **250**	**80.1** **71.3** **40.2**	**This work**

Table S3. Comparison of the thickness and electrochemical performances based on interphase layer incorporation for anode-free Li metal batteries.

Anode	Interphase layer thickness (μm)	Area capacity (mAh cm^{-2})	Cycle number	Capacity retention (%)	Ref.
Li-SiOx /Cu	23	1.1	200	~20	3
PVDF-Cu	1	1.56	30	61.45	18
Cu-Ag@PDA-GO	9.6	2.23	80	65.4	22
Cu@PEO	1.5	0.71	100	49.6	23
Cu@LLCZN/PVDF	2	2.13	30	58.6	24
Cu@GO	1.15	2	100	48	25
TEG-Cu	**0.25**	**3**	**100**	**80.1**	**This work**
			150	**71.3**	
			250	**40.2**	

Supporting References

[1] Wang Y., *Adv. Funct. Mater.* **2020**, *30*, 2000373.

[2] Ryou M., *Energy Environ. Sci.* **2022**, *15*, 2581–2590.

[3] Chen W., *et al*, *Adv. Mater.* **2020**, *32*, e2002850.

[4] Heubner C., *et al*, *Adv. Energy Mater.* **2021**, *11*, 2102647.

[5] Cheng X., *et al*, *Nat. Commun.* **2017**, *8*, 336.

[6] Yan C., *et al*, *Angew. Chem. Int. Ed.* **2018**, *57*, 14055-14059.

[7] Tan S., *et al*, *Angew. Chem. Int. Ed.* **2019**, *58*, 7802-7807.

[8] Zheng H., *et al*, *Adv. Energy Mater.* **2020**, *10*, 2001440.

[9] Xu Y., *et al*, *Matter* **2020**, *3*, 1685-1700.

[10] Shi P., *et al*, *Adv. Funct. Mater.* **2021**, *31*, 2004189.

[11] Holoubek J., *et al*, *ACS Energy Lett.* **2020**, *5*, 1438-1447.

[12] Li S., *et al*, *Nat. Nanotech.* **2022**,*17*, 613-621.

[13] Nanda S., *et al*, *Adv. Energy Mater.* **2021**, *11*, 2000804.

[14] Qian J., *et al*, *Adv. Funct. Mater.* **2016**, *26*, 7094-7102.

[15] Yu Z., *et al*, *Nat. Energy* **2022**, *7*, 94-106.

[16] Rodriguez R., *et al*, *ACS Appl. Energy Mater.* **2018**, *1*, 5830-5835.

[17] Brown Z. L., *et al*, *J. Electrochem. Soc.* **2019**, *166*, A2523-A2527.

[18] Abrha L. H., *et al*, *ACS Appl. Energy Mater.* **2021**, *4*, 3240−3248.

[19] Li Z., *et al*, *Energy Stor. Mater.* **2022**, *45*, 40-47.

[20] Beyene T. T., *et al*, *ACS Appl. Mater. Interfaces* **2019**, *11*, 31962-31971.

[21] Xu R., *et al*, *Adv. Mater.* **2021**, *33*, e2105962.

[22] Wondimkun Z. T., *Energy Stor. Mater.* **2021**, *35*, 334–344.

[23] Assegie A. A., *et al*, *Nanoscale* **2018**, *10*, 6125.

[24] Abrha L. H., *et al*, *Electrochim. Acta* **2019**, *325*, 134825.

[25] Wondimkun Z. T., *et al*, *J. Power Sources* **2020**, *450*, 227589.